PNAS

Main Manuscript for

Accumulated 3-phosphoglycerate in darkness is a primary starting substrate for stepwise photosynthetic induction process in cyanobacteria

Kenya Tanaka[1,2], Tomokazu Shirai[3,4], Mami Matsuda[4], Akihiko Kondo[1,3,4,5], Tomohisa Hasunuma[1,3,4,*]

1. Engineering Biology Research Center, Kobe University, 1-1 Rokkodai, Nada, Kobe 657-8501, Japan

2. Research Center for Solar Energy Chemistry, Graduate School of Engineering Science, Osaka University, Toyonaka, Osaka 560-8531, Japan

3. RIKEN Center for Sustainable Resource Science, 1-7-22 Suehiro-cho, Tsurumi-ku, Yokohama, Kanagawa 230-0045, Japan

4. Graduate School of Science, Innovation and Technology, Kobe University, 1-1 Rokkodai, Nada, Kobe 657-8501, Japan

5. Department of Chemical Science and Engineering, Graduate School of Engineering, Kobe University, 1-1 Rokkodai, Nada, Kobe 657-8501, Japan

*Corresponding author: Tomohisa Hasunuma

Email: hasunuma@port.kobe-u.ac.jp

Author Contributions: K.T. and T.H. designed the research. K.T. and M.M. performed research. K.T. and T.S. analyzed data. K.T., T.S., A.K. and T.H. wrote the article.

Competing Interest Statement: The authors declare no competing interests.

Preprint Servers: bioRxiv; https://doi.org/10.1101/2022.04.04.486922

Classification: BIOLOGICAL SCIENCES; Plant Biology

Keywords: Photosynthetic induction, Calvin-Benson-Bassham cycle, Metabolic flux analysis, CO_2 fixation, 3-phosphoglycerate

This PDF file includes:

Main Text
Figures 1 to 5

Abstract

In photosynthetic organisms, a smooth metabolic transition from dark to light conditions is essential for efficient CO_2 fixation and growth. Dark-to-light transition leads to activation of the enzymes of the Calvin-Benson-Bassham (CBB) cycle and initiates CO_2 fixation metabolism using energy and redox equivalents provided by the photosynthetic electron transfer reaction. While many enzymatic mechanisms of the light activation of the CBB cycle have been clarified to date, the metabolic distribution and dynamics underlying the smooth start of photosynthetic metabolism remain unclear. Here, we show rapid (on a time scale of seconds) dynamics of changes in absolute metabolite concentration and ^{13}C tracer incorporation during photosynthetic induction (PI) in the cyanobacterium *Synechocystis* sp. PCC 6803. By combining these data, we were able to estimate time-resolved nonstationary dynamics of metabolic fluxes during PI. This novel metabolic analysis indicated that the initial step of PI consists of the reduction of 3-phosphoglycerate (3PG), a metabolite that accumulates in dark conditions; This step occurs before the subsequent generation of ribulose-1,5-bisphosphate (RuBP) and CO_2 fixation by ribulose-1,5-bisphosphate carboxylase/oxygenase (Rubisco). *In vivo* oxygen evolution measurement in the presence of a CBB cycle inhibitor further confirmed that the accumulated 3PG is a major initial substrate for RuBP generation and that 3PG functions as a key electron sink before the initiation of CO_2 fixation. Our results thus illustrate a fundamental mechanism supporting the seamless activation of photosynthetic metabolism after dark-to-light transitions.

Significance Statement

Plants, algae and cyanobacteria activate photosynthetic CO_2 fixation after transition from dark to light conditions. Although this metabolic regulation is the fundamental system which enables photosynthetic organisms to grow in fluctuating light environment, metabolite distribution and dynamics essential for smooth initiation of photosynthetic metabolism remain unclear. Here we determined nonstationary metabolic flux dynamics during photosynthetic induction by quantifying changes in absolute metabolite concentrations at second-scale time intervals after the dark-to-light transition in cyanobacteria. This novel metabolic analytical technique revealed that 3-phosphoglycerate that has accumulated in the dark period is a primary starting substrate for fast ribulose 1,5-bisphosphate generation and the subsequent initiation of CO_2 fixation. This metabolic principle can be used for constructing efficient chemical production systems using CO_2 fixation.

Main Text
Introduction

In leaves and isolated chloroplasts, there is known to be a delay between the onset of illumination and achieving a maximum rate of photosynthetic CO_2 fixation (1). Since this photosynthetic induction (PI) process was suggested more than a century ago (2), the underlying mechanisms have been investigated intensively. Since the 1960s, the activation processes of many of the enzymes in the Calvin-Benson-Bassham (CBB) cycle have been studied(3), including those of glyceraldehyde 3-phosphate dehydrogenase (GAPDH), fructose-1,6-bisphosphatase (FBPase), sedoheptulose-1,7-bisphosphatase (SBPase), phosphoribulokinase (PRK), and ribulose-1,5-bisphosphate carboxylase/oxygenase (Rubisco). The activities of these enzymes are known to be altered by changes in cellular environmental properties such as redox state, energy charge, and ion concentration; these changes themselves reflect the effects of the photosynthetic electron transfer reaction (4–6). Eventually, an overview of the PI process in the leaves of terrestrial plants was developed, and can be summarized as follows: enzymes of RuBP regeneration pathways

are activated in the first 1-2 min of illumination, followed by completion of slower Rubisco activation and stomatal opening within 7 to 10 min (7).
In addition to these enzymatic mechanisms, recent analyses performed using a theoretical photosynthetic model have predicted that maintaining the appropriate concentrations of CBB cycle intermediates is crucial for the initiation of CO_2 fixation (8). Experimental evidence in cyanobacteria has confirmed that the transfer of the carbon supply from a storage polymer (glycogen) to the CBB cycle affects photosynthetic efficiency (9, 10).
However, details of the metabolic distribution and metabolic flux dynamics that are essential for efficient PI remain unknown. This shortcoming likely reflects the fact that the metabolic change during PI is poorly understood. Although transient changes in metabolite levels have been reported during PI in algae, in the chloroplasts of spinach protoplasts, and in wheat and maize leaves (11–15), we have yet to obtain systematic understanding of metabolite dynamics due to the lack of comprehensive and quantitative analyses. Instead, the metabolic dynamics and stability of the CBB cycle have been analyzed by computational modeling using random sampling of kinetic parameters instead of using known metabolomes and flux distribution as a basis for model parameterization, given the lack of such analyses (16).
Among oxygenic photosynthetic organisms, cyanobacteria are the only prokaryotes; notably, in this class of organisms, most metabolic reactions are performed in a shared space, the cytoplasm. Thus, it is not obvious that the metabolic dynamics of PI in cyanobacteria is similar to that in leaves and chloroplasts. On the other hand, cyanobacteria fix CO_2 via the CBB cycle like that used in higher plants, and these prokaryotes are regarded as the likely ancestor of the plant chloroplast (17). Despite its importance for further understanding PI processes across photosynthetic organisms, cyanobacterial metabolic dynamics during PI have not (to our knowledge) been studied to date.
The ideal way to systematize complicated metabolic changes during PI is to estimate metabolic flux changes, which represent the integrated network responses of enzymes and metabolites. Analysis of metabolic fluxes provides useful information regarding topics such as pathway bottlenecks and network regulation in biological systems (18). Although metabolic flux analysis (MFA) using an isotope tracer enables the mapping of intracellular carbon fluxes (19), the approach cannot be applied to a metabolically nonstationary state where metabolic fluxes and pool sizes are variable. On the other hand, previously developed dynamic MFA, which incorporates specialized statistical approaches, has permitted the estimation of long-term flux changes over the culture interval (20, 21). There has been (to our knowledge) no appropriate approach for the quantitative determination of metabolic flux change in short, metabolically transient states, including that of PI.
To estimate nonstationary metabolic flux changes, the following relationship was employed. The accumulation rate of a metabolite in a metabolic network is defined as the sum of all fluxes producing that metabolite minus the sum of all fluxes consuming that metabolite, as represented in following equation:

$$r_i(\mathrm{t}) = \sum_j \alpha_j x_j(t) - \sum_k \alpha_k x_k(t) \qquad (1)$$

where, $x_j(t)$ is the flux through reaction *j*, α_j is a stoichiometric coefficient, and $r_i(\mathrm{t})$ is the accumulation rate of metabolite *i* (22). An example of three fluxes is illustrated in Fig. 1A. To obtain accumulation rates for estimation of the flux values, it is necessary to examine the absolute concentration change of metabolites with high time resolution. Namely, the metabolic flux during PI can be calculated by quantifying the change in metabolite concentration over highly time-resolved intervals immediately following light irradiation.

The time-resolved absolute quantification during PI in cyanobacteria has not been performed to date due to the technical difficulties of absolute quantification and rapid sampling. Here, by developing the integrated process shown in Fig. 1B, we successfully quantified absolute metabolite concentration changes at second-scale intervals during PI in the cyanobacterium *Synechocystis* sp. PCC 6803 (hereafter *Synechocystis*). Additionally, to identify active metabolic pathways during PI, ^{13}C labeling dynamics after initiating light irradiation were analyzed (Fig. 1C). These accurate concentration and labeling dynamics allowed us to conduct short-time dynamic

metabolic flux analysis (STD-MFA) and to estimate nonstationary flux change during PI. These analyses demonstrated a stepwise activation behavior that supports the smooth start of photosynthetic metabolism in *Synechocystis*.

Results

Absolute concentration changes in central carbon metabolic pathways during PI. Firstly, we sought to determine the absolute concentration dynamics of intermediate metabolites in central energy metabolism during PI in *Synechocystis*. As light irradiation rapidly causes metabolic variation driven by increases in ATP and NADPH via the photosynthetic electron transfer reaction, rapid sampling and quenching of cellular metabolic activity are necessary for detecting metabolic changes during PI. A standardized procedure for intracellular metabolome quantification requires multiple analytical steps, including quenching of microbial metabolic activity, separation of microbial cells from growth medium, and extraction of intracellular metabolites, followed by mass spectrometric metabolite analysis. These multistep processes largely impede accurate estimation of the '*in vivo*' cellular metabolic state. Typically, metabolic activities are stopped rapidly by adding a quenching solution, such as a cold methanol solution, followed by harvesting cells. However, metabolite leakage in the quenching solution is known to interfere with precise quantification of metabolite levels (23). Although quick filtration usually is used for rapid cell sampling before quenching and extraction processes, the '*in vivo*' metabolic state may change markedly due to variation in the light environment during the filtration process in the case of photosynthetic microorganisms. Furthermore, extraction yields of water-soluble metabolites depend on the extraction solvent, given that such metabolites may decompose during extraction processes (24). The exact determination of metabolite concentrations also is hampered by ion-suppression effects during mass spectrometric analysis (25).

To overcome these problems, in the present study, we employed a combination of two strategies. Firstly, to analyze intracellular metabolites, cells were separated from growth medium and suspended in 1 mM $NaHCO_3$ prior to metabolite sampling. This allowed quenching and extraction of intracellular metabolites merely by directly dropping the cell suspension into the extraction solution during light irradiation, and avoided metabolic state variation during the sampling process. We chose phenol-chloroform-isoamyl alcohol (PCI) solution (pH 7.9) as an extraction solution because PCI extraction enabled rapid and efficient extraction of NADPH from *Synechocystis* (26). Note that the exchange of medium for $NaHCO_3$ solution is a typical pretreatment for measuring photosynthetic activity of fresh-water cyanobacteria (27). Secondly, stable isotopomers of the analyte compounds were used as an internal standard (IS). Although experimental protocols using the isotope-labeled IS have been developed for absolute quantification of metabolite concentrations in various microorganisms including cyanobacteria (28–31), few attempts (to our knowledge) have been made to apply this accurate quantification method to time course analysis.

Figure 1B shows the experimental process for the exact determination of the absolute metabolite concentration dynamics of PI. We prepared a ^{13}C-labeled IS mixture by extracting metabolites from *Synechocystis* cells cultivated with $NaH^{13}CO_3$ as the sole carbon source. Absolute concentrations of uniformly ^{13}C-labeled metabolites were determined using capillary electrophoresis-mass spectrometry (CE-MS) based on the ratio between peak areas of known concentrations of unlabeled compounds included as an IS and the uniformly ^{13}C-labeled metabolites. Then, to quantify absolute concentration change during PI, dark-adapted *Synechocystis* cells (grown in darkness for 12 h) were illuminated at a light intensity of 30 μmol m^{-2} s^{-1} (the same as the growth light intensity) or 200 μmol m^{-2} s^{-1}. Metabolites of these cells were extracted rapidly using PCI solvent containing the ^{13}C-labeled extract as a labeled IS whose concentration was determined using another aliquot in the same extraction batch. Importantly, because of the high physicochemical similarities between the labeled IS and the unlabeled analyte, the two mixtures undergo similar opportunities for degradation and ion suppression effects, permitting compensation for the above drawbacks (28–31). Given that the absolute metabolite concentrations were determined based on the ratio between unlabeled and uniformly labeled peak areas (Fig. 1B), the process was expected to prevent contamination of unlabeled metabolites in the ^{13}C-labeled IS. The

proportions of uniformly ^{13}C-labeled metabolites (compared to sum of unlabeled and uniformly labeled metabolites) were found to exceed 95% for all metabolites except for citrate (*SI Appendix*, Fig. S1). Figure 2 shows the temporal changes in the absolute metabolite concentration after the initiation of light irradiation at 30 μmol m^{-2} s^{-1} or 200 μmol m^{-2} s^{-1}. It should be noted that a small amount of some metabolites was extracellular (*SI Appendix*, Fig. S2). A previous study that measured NADPH fluorescence *in vivo* revealed that the amount of NADPH in *Synechocystis* increased within 0.5 s of illumination (32). The rapid increase of NADPH observed within 5 s in the present work was consistent with that of an earlier *in vivo* study (32), confirming that this metabolomics analysis successfully detected the rapid start of photosynthesis. As with NADPH, the level of the energy cofactor ATP also increased rapidly. Overall, the levels of 3-phosphoglycerate (3PG), 2-phosphoglycerate (2PG), and phosphoenolpyruvate (PEP) decreased; the levels of other CBB cycle intermediates (excepting 3PG, ribulose 5-phosphate (Ru5P) and xylulose 5-phosphate (Xu5P)) increased, while the levels of tricarboxylic acid (TCA) cycle intermediates did not change appreciably. Considering these metabolite variations together, we inferred that accumulated glycolysis intermediates including 3PG, 2PG, and PEP likely were converted to CBB cycle intermediates at the initial step of PI.

^{13}C labeling kinetics during PI. A direct way to confirm this hypothesis is to determine the metabolic flux distribution at PI. However, the precise metabolic flux values cannot be determined when the number of unknown flux parameters is larger than that of known metabolite concentration changes in the metabolic model system used for flux calculation. To perform STD-MFA, we sought to refine the metabolic model by excluding metabolic pathways that are inactive during PI. However, the metabolite concentration data in Fig. 2 cannot identify the inactive metabolic pathways. Notably, even if the metabolic concentration change is zero, metabolic flux is not necessarily zero, because such an observation instead may indicate that metabolic inflow and outflow are balanced. In the case where the concentration of a metabolite is stable and ^{13}C is not incorporated into the metabolite during photosynthetic $^{13}CO_2$ fixation, the metabolic fluxes around the metabolite are estimated to be very small, and so can be neglected. Therefore, we next measured the dynamics of ^{13}C isotope incorporation after the transition from dark to light conditions by starting photosynthesis while the cells were suspended in a solution of $NaH^{13}CO_3$. Figure 3 shows the time courses of the transient changes in the atomic fraction of labeled carbon. In contrast to the high ^{13}C fraction seen for CBB cycle intermediates, 6-phosphogluconate (6PG) and TCA cycle intermediates (except for malate and fumarate) were not labeled. In addition, the ^{13}C fraction of ADP-glucose, which is known to be a precursor of glycogen (33), was low. When these results were considered together with those indicating that the concentrations of these metabolites did not change appreciably during PI (Fig. 2), we inferred that the metabolic fluxes in the TCA cycle, the oxidative pentose phosphate pathway (OPPP), the Entner-Doudoroff pathway (EDP), and the glycogen synthesis pathway are extremely low immediately after light irradiation.

Other than Rubisco, the primary metabolic enzymes that incorporate CO_2 are phosphoenolpyruvate carboxylase (PepC) and malic enzyme (ME), which are directly or indirectly connected to malate (Fig. 3). Since malate was not labeled until 60 s after the initiation of light irradiation (at both of the tested light intensities), ^{13}C incorporation before 60 s was inferred to reflect Rubisco activity. The amount of incorporated ^{13}C atom was calculated by multiplying the measured ^{13}C fraction (shown in Fig. 3) by the absolute carbon concentration of each metabolite (shown in Fig. 2); these analyses are presented in *SI Appendix*, Fig. S3*A* and *B*. The total amount of incorporated ^{13}C atom was derived by summing the number of ^{13}C atoms of all measured metabolites (*SI Appendix*, Fig. S3*C*, *D*). Notably, ^{13}C incorporation did not start until 12 s after the initiation of light irradiation. On the other hand, ^{13}C incorporation was observed at least 10 s after the addition of $NaH^{13}CO_3$ to cells whose photosynthetic activity already had been activated by 5 min of illumination (*SI Appendix*, Fig. S4). Together, these results suggested that the observed delay in the start of ^{13}C incorporation (compared to the start of light irradiation) was not attributable to slow uptake of $NaH^{13}CO_3$ by the cells. Instead, these data indicated that the fixation of CO_2 through Rubisco remains inactive at the initial stage of photosynthetic metabolism (i.e., immediately following the start of illumination). Although the delayed onset of CO_2 fixation is a well-known phenomenon in plant leaves (1), this

observation in the present work is (to our knowledge) the first direct demonstration of a Rubisco activation effect in the *in vivo* metabolic dynamics in cyanobacteria.
It is interesting to note that labeled carbon was incorporated into malate and fumarate after 120 s, particularly in cells illuminated at 200 μmol m^{-2} s^{-1}, at a time when other TCA cycle intermediates remained unlabeled. This result suggested that malate and fumarate are generated by the reductive TCA pathway, which is known as a fermentation pathway employed for NADH oxidation (34). Thus, the accumulation of NADH may drive the activity of this reductive TCA pathway (*SI Appendix*, Fig. S5).

Short-term dynamic metabolic flux analysis (STD-MFA). Finally, we calculated temporal changes in the net metabolic fluxes based on the obtained data. As mentioned above, during the first 60 s of illumination, the net metabolic fluxes in pathways other than the CBB cycle and glycolysis until 60 s appeared to be very small. In fact, the concentrations of newly synthesized (labeled) amino acids before 60 s were hardly changed, even in cells illuminated at 200 μmol m^{-2} s^{-1}, although the labeled levels of some amino acids (serine, alanine, phenylalanine, tyrosine and ornithine) increased significantly after the first minute of illumination (*SI Appendix*, Fig. S6). Furthermore, photorespiratory intermediates such as glycolate, glyoxylate and glycerate did not accumulate during the first 60 s of illumination (*SI Appendix*, Fig. S7). Therefore, we assessed the metabolic pathways shown in *SI Appendix*, Fig. S8*A* as part of the subsequent calculations, focusing on metabolic dynamics during the first 60 s following the initiation of illumination.

To solve equation (1) and conduct STD-MFA, accumulation rates for metabolites in the metabolic model shown in *SI Appendix*, Fig. S8*A* were derived from the slopes obtained between two consecutive concentration data points in Fig. 2. In addition to our use of equation (1), we calculated the CO_2 fixation rate as the increase in the rate of total ^{13}C incorporation (*SI Appendix*, Fig. S3). Specifically, the latter parameter was interpreted as the metabolic flux from RuBP to 3PG, given that the ^{13}C incorporation experiment mentioned above indicated that all carbon atoms fixed during the first 60 s of illumination were attributable to Rubisco activity. The net metabolic fluxes of each time interval were estimated by solving these equations simultaneously (Fig. 4, *SI Appendix*, Fig. S8). The estimated flux values were validated and judged to be reliable, given that almost all of the estimated metabolite accumulation rate values (which were derived from the estimated fluxes) yielded values that were within the mean ± SD range of the measured accumulated rate (*SI Appendix*, Fig. S9). For more details of the calculation process and equations, see the Methods section.

The time course of flux distribution clearly indicated that photosynthetic metabolism in *Synechocystis* starts in a stepwise manner: first, activation of the reduction of 3PG to glyceraldehyde 3-phosphate (GAP); second, generation of RuBP; and third, Rubisco activation (Fig. 4, *SI Appendix*, Fig. S8*C*, *D*). Interestingly, the induction of RuBP generation can be further divided into two sub-steps based on metabolic fluxes, given that the formation fluxes of C6 intermediates (fructose 1,6-bisphosphate (FBP) and fructose 6-phosphate (F6P)) increased faster than that of C7 intermediates (sedoheptulose 1,7-bisphosphate (SBP) and sedoheptulose 7-phosphate (S7P)) (*SI Appendix*, Fig. S8*C*, *D*). Notably, the C6 and C7 pathways share an enzyme, fructose-1,6-bisphosphatase, which (in *Synechocystis*) is known to be a bi-functional fructose-1,6-/sedoheptulose-1,7-bisphosphatase (FBP/SBPase) (35). Thus, modification of enzymatic activity is unlikely to be the cause of the activation time gap between the two pathways. In the CBB cycle, the production of erythrose 4-phosphate (E4P), a starting substrate of the C7 pathway, depends on the activity of the C6 pathway. Therefore, we inferred that substrate deficiency in the C7 pathway is attributable to the metabolic pathway topology in the CBB cycle, delaying the C7 pathway relative to the C6 pathway in *Synechocystis*.
The reduction fluxes of 3PG differed greatly between cells illuminated at 30 and 200 μmol m^{-2} s^{-1}, even before the initiation of CO_2 fixation (i.e., during the first 5-20 s) (Fig. 4). In steady-state photosynthesis, the increased rate of electron donor (NADPH) production from the photosynthetic electron transfer reaction at the higher light intensities is balanced by the rate of electron acceptor (3PG) production that also is increased by the elevated CO_2 fixation rate. On the other hand, before the onset of CO_2 fixation that follows the initiation of light irradiation, excess reducing power can be

accumulated because 3PG cannot be produced while NADPH is produced by the electron transfer reaction. Nevertheless, the increase in the reducing fluxes of 3PG with the higher light intensity (200 μmol m^{-2} s^{-1}) before CO_2 fixation suggests that, even before the onset of CO_2 fixation, the rate of 3PG consumption is balanced by the rate of NADPH production rate from the electron transfer reaction, which varies with light intensity. In addition, it can clearly be seen that 2PG and PEP were converted to 3PG at the both light intensities (Fig. 4). Therefore, we proposed that the accumulation of these glycolytic intermediates provides a "stand-by" state and flexibility for the initiation of photosynthetic metabolism before the start of CO_2 fixation; thus, these intermediates are expected to play an important role in balancing cofactor regeneration and consumption during PI.

Oxygen evolution in the presence of a CBB cycle inhibitor. To confirm the function of 3PG as an electron acceptor at the start of photosynthesis *in vivo*, we measured the oxygen evolution rate in the presence of a CBB cycle inhibitor, glycolaldehyde (GA). GA is known to inhibit the conversion of triose phosphate to RuBP in the CBB cycle, thereby impeding oxygen evolution during steady-state photosynthesis in cyanobacteria (36). If 3PG serves as an electron acceptor for the NADPH generated by the photosynthetic electron transfer reaction, then oxygen evolution in light-exposed, GA-treated cells should proceed only until the accumulated 3PG is exhausted. As expected, GA-treated cells generated oxygen starting just after the initiation of illumination, but oxygen evolution by these cells diminished rapidly after 25 s of irradiation under 200 μmol m^{-2} s^{-1} light (Fig. 5A). Based on theoretical stoichiometry, two molecules of NADPH produced by one molecule of evolved oxygen reduce two molecules of 3PG. The total decreasing rate of 3PG, 2PG and PEP immediately after irradiation with light at 200 μmol m^{-2} s^{-1} was approximately twice that of the oxygen evolution rate in GA-treated cells (Fig. 5A, C). This quantitatively supports that the accumulated glycolytic metabolites acted as electron acceptors for evolved oxygen in GA-treated cells. Moreover, the oxygen evolution rate of GA-treated cells from the onset of the 200 μmol m^{-2} s^{-1} illumination to 25 s was identical to the rate of oxygen evolution from non-treated cells (Fig. 5A). This suggests that even in a normal PI process in non-GA-treated cells, the electron acceptors that contribute to the initial oxygen evolution in PI are the accumulated glycolytic intermediates. In cells irradiated with 30 μmol m^{-2} s^{-1} light, no significant difference in oxygen evolution rate dynamics was observed between GA-treated and non-treated cells; this effect presumably reflected slow consumption and depletion of 3PG in GA-treated cells (Fig. 5B, D). To confirm our hypothesis, we demonstrated depletion of 3PG and inhibition of RuBP accumulation in GA-treated cells following irradiation with 200 μmol m^{-2} s^{-1} light (*SI Appendix*, Fig. S10). These results clearly indicated that accumulated 3PG functions as a first electron acceptor for the rapid initiation of photosynthetic metabolism upon exposure of dark-adapted cyanobacteria to light.

Discussion

In the present study, combined analysis of absolute metabolite concentrations and isotope incorporation transients of a wide spectrum of metabolites permitted us to visualize changes in nonstationary metabolic fluxes during PI in *Synechocystis*. The activation order during PI in *Synechocystis* was found to be resemble that in terrestrial plants, where the activation of RuBP generation typically precedes the start of CO_2 fixation (7). However, the detailed order of activation of the various pathways in plant leaves has not (to our knowledge) been investigated. STD-MFA revealed that the step of activation of RuBP generation in *Synechocystis* involves two phases, the fast C6 pathway and the slower C7 pathway. This distinction in timing was inferred to reflect the metabolic pathway topology inherent to the CBB cycle. Furthermore, 3PG accumulated in the dark period was found to be depleted rapidly, apparently functioning as a starting substrate for RuBP generation before the start of CO_2 fixation. This rapid depletion of phosphoglycerate upon illumination also has been observed in algae, in the chloroplast of spinach protoplasts, and in the leaves of a C3 plant (wheat) (11, 12, 15). In contrast, monotonic accumulation of phosphoglycerate has been reported in the leaves of a C4 plant (*Zea mays*) (13, 14). We suspect that the difference in phosphoglycerate dynamics during PI may reflect divergence between C3 and C4 photosynthetic metabolism, but clearly further investigation is necessary.

A closer look at Fig. 2 permits a more detailed characterization of the details of the individual metabolic pathways. Although increases in the levels of NADPH and ATP (which occur within 5 s of the start of illumination) should make the reduction of 3PG to GAP energetically favorable, a large decrease in the level of 3PG is observed after the 5-s time point. Cyanobacterial phosphoglycerate kinase (PGK) and GAPDH are activated by reductive dissociation of cysteine pairs upon light illumination (37, 38). Thus, the delay in 3PG consumption until after 5 s of illumination likely is due to the need for the redox activation of PGK and GAPDH. Transient accumulation of FBP indicates the existence of an activation period for the FBP/SBPase enzyme. FBP/SBPase in *Synechocystis* is activated by the reduction of a thiol group and binding of Mg^{2+}, and this enzyme is inhibited allosterically by the binding of AMP (39, 40). Indeed, a rapid decrease in AMP concentration was confirmed after light irradiation (*SI Appendix*, Fig. S5). In addition, temporal accumulation of dihydroxyacetone phosphate (DHAP) upon irradiation with 200 μmol m^{-2} s^{-1} light may be attributable to the transient rate-limitation of FBP/SBPase. The significantly higher continuous accumulation of F6P and S7P in cells illuminated at 200 μmol m^{-2} s^{-1} (compared to those illuminated at 30 μmol m^{-2} s^{-1}) indicates that the reaction catalyzed by the transketolase enzyme is the major rate-limiting step. This interpretation is consistent with the results of a previous study, which reported enhanced photosynthetic activity in a *Synechocystis* strain engineered to overproduce transketolase (41). Regarding RuBP dynamics, *Synechocystis* (like plants) requires Rubisco activation processes, although the mechanism of this activation differs slightly between these two classes of organisms (42). Thus, the accumulation and subsequent decrease of RuBP in cyanobacteria suggests a phase shift from inactivated to activated Rubisco. Indeed, similar dynamics of the RuBP pool size has been observed during PI in plant leaves, and is associated with Rubisco activation (43, 44). The levels of GAP, E4P, and ribose 5-phosphate (R5P) were below the detection limit, suggesting that these metabolites are consumed rapidly and are not accumulated during PI. The levels of 2PG and PEP decreased more slowly than those of 3PG. Phosphoglycerate mutase catalyzes the reversible conversion between 3PG and 2PG, while enolase catalyzes the reversible conversion between 2PG and PEP. To assess the direction of these processes, the reaction Gibbs energy change ($\Delta_r G$) of these reactions was calculated based on following equation:

$$\Delta_r G = \Delta_r G^{\circ} + RT \ln Q \tag{2}$$

$$Q_{3PG \to 2PG} = \frac{[2PG]}{[3PG]}, Q_{2PG \to PEP} = \frac{[PEP]}{[2PG]}$$

where, $\Delta_r G^{o}$ is the standard reaction Gibbs energy change, R is the ideal gas constant, T is the temperature, and Q is the reaction quotient. As the conversions among 3PG, 2PG, and PEP are simple reactions, where one reactant species is converted to one product (along with water), consideration of cell volume is not necessary, allowing relatively precise estimation of $\Delta_r G$. Therefore, we focused on the $\Delta_r G$ estimation of these reactions. Corresponding $\Delta_r G^{o}$ values were obtained as the means of the experimentally determined values summarized in Bennett et al. (29). The changes in reaction Gibbs energy from 3PG to 2PG and from 2PG to PEP during the first 60 s of light irradiation were either positive values or approximately zero (*SI Appendix*, Fig. S11). These analyses are consistent with our inference that the direction of net metabolic flux is from PEP to 3PG immediately following the initiation of light irradiation, as shown in Fig. 4.

Let us consider the mechanisms by which large amounts of 3PG are accumulated in dark-adapted *Synechocystis*. Cyanobacteria utilize glycogen stored during the day for respiratory metabolism at night. In mutant strains deficient in the synthesis or degradation of glycogen, the activation of photosynthetic metabolism is delayed due to the lack of CBB cycle intermediates (9, 10). On the other hand, the enzymatic activities of the TCA cycle in *Synechocystis* are known to be lower than those in other organisms (45). Thus, we infer that the generation of glycolytic intermediates by glycogen degradation and slow catabolic activity via TCA cycle are likely to cause the accumulation of 3PG along with 2PG and PEP in dark-adapted *Synechocystis*.

The STD-MFA technique developed in this study is a method for quantifying changes over time of metabolic flux during a dynamic phenomenon that induces rapid metabolic changes that occur over short intervals (within a few minutes). This method requires the measurement of time-resolved absolute concentration changes and metabolic model refinement based on isotope

incorporation data before flux calculation. Previously developed dynamic metabolic flux analysis methods typically are intended to estimate flux change over long periods of culture processes, and require technically specialized mathematical approaches (20, 21). In contrast, STD-MFA permits the direct determination of metabolic flux changes in exchange, albeit while focusing on short time intervals. We expect that this method also may be of use for understanding other non-stationary rapid metabolic changes that have been the recent focus of attention, such as the end of photosynthesis and adaptation against oxidative stress (46, 47).
We have demonstrated that the accumulation of glycolysis intermediates smoothens metabolic initiation of the CBB cycle in *Synechocystis*. The rational metabolic engineering methods based on the findings presented in this study may improve CO_2 fixation rate and growth of synthetic autotrophic microorganisms, which require further metabolic optimization (48, 49). Such methods may facilitate the construction of efficient bio-based chemical production from CO_2.

Materials and Methods

Growth conditions

This work employed a glucose-tolerant wild strain of *Synechocystis* (50) that was grown and stored on solid BG-11 media plates containing 1.5% Bacto agar. Pre-culturing was performed in 200-mL flasks containing 50 mL each of liquid BG-11 medium buffered with 20 mM 2-[4-(2-hydroxyethyl)-1-piperazinyl]ethanesulfonic acid (HEPES, pH 7.5); each flask was inoculated with cells harvested from the agar plates. These flasks then were cultured at 30 ºC in ambient air with shaking at 100 rpm; illumination at an intensity of 30 µmol $m^{-2}s^{-1}$ was provided by white light-emitting diode (LED) lights. The main culture was initiated by adding pre-culture grown for 4 days into 70 mL of the BG-11 medium to give an optical density of 0.05 at 730 nm (OD_{730}). The growth condition of the main culture was the same as that of the pre-culture. The dry cell weight (DCW) was measured after harvesting cells by centrifugation and lyophilization. The obtained relationship between the OD_{730} value and DCW ($DCW = 0.1998 \times OD_{730} \times V + 0.0974$; $R^2=0.982$; n=9; V is volume of cell suspension) was used for estimating DCW from the OD_{730} value.

Preparation of ^{13}C isotope-labeled internal standard (^{13}C-IS)

Synechocystis cells in pre-culture were inoculated to an OD_{730} of 0.05 in a serum bottle containing 60 mL modified BG-11 medium supplemented with 100 mM HEPES (pH 7.5) and 25 mM $NaH^{13}CO_3$ (in place of the unlabeled Na_2CO_3 included in the standard BG-11 medium). The culture serum bottle was sealed, followed by flushing with N_2 gas to remove unlabeled ambient CO_2. The growth conditions used for the labeled culture were the same as those used for the pre-culture and main culture. Cells grown for 3 days were harvested and re-suspended in fresh modified BG-11 to avoid pH increase during cultivation with $NaH^{13}CO_3$ as the sole carbon source. The labeled culture then was grown under the same conditions for another 3 days, followed by extraction of uniformly labeled metabolites, as described below.
The entire volume of the labeled culture was harvested by centrifugation, washed with 1 mM $NaH^{13}CO_3$ solution, and then re-suspended in 9 mL of 1 mM $NaH^{13}CO_3$. The resulting cell suspension was illuminated for 90 s with white LED light at an intensity of 200 µmol $m^{-2}s^{-1}$ (to maximize extraction yield of CBB cycle intermediates), and placed into a mixture of 9 mL PCI (pH 7.9, Nacalai Tesque, Kyoto, Japan) and 60 µL 0.5 M N-cyclohexyl-3-aminopropanesulfonic acid (CAPS, pH 10.6) for metabolite extraction. The extraction mixture was centrifuged at 4 ºC at 8,000 $\times g$ for 3 min. Twelve to 13 fractions of the water layer were then aliquoted into microtubes and lyophilized.
One of the dried aliquots was dissolved in 20 µL of standard mixture containing prepared unlabeled compounds. The sample was analyzed by capillary electrophoresis-mass spectrometry (CE-MS) (CE, Agilent G7100; MS, Agilent G6224AA LC/MSD TOF; Agilent Technologies, Palo Alto, CA, USA) as described previously (51). Absolute concentrations of the uniformly labeled isotopomer (C_n) were derived as follows:

$$C_n = \frac{S_n}{S_0} C_0 \tag{3}$$

where, S_n and S_0 are the peak areas of uniformly ^{13}C-labeled (namely, the number of ^{13}C atoms in a *n*-carbon compound is equal to *n*) and unlabeled standard signals, respectively, and C_0 is the prepared concentration of the unlabeled standard.

Metabolite extraction with rapid sampling and analysis

To perform metabolite sampling for analyses of absolute concentration and ^{13}C incorporation after the transition from dark to light, a main culture grown for 6 days was dark-adapted for 12 h. A calculated volume (90/OD_{730}, in mL) of the dark-adapted cell culture was harvested by centrifugation at 8000×*g* for 5 min. The cells were washed with 4 mL of 1 mM $NaHCO_3$ (for absolute concentration analysis) or 1 mM $NaH^{13}CO_3$ (for ^{13}C incorporation analysis), and harvested again by centrifugation. The washed cells were resuspended in 6.8 mL of 1 mM $NaHCO_3$ (for absolute concentration analysis) or 1 mM $NaH^{13}CO_3$ (for ^{13}C incorporation analysis). Nine aliquots (750 µL each) of the resulting cell suspension were then loaded into clear pipet tips (*SI Appendix*, Fig. S12). Up to this point, light irradiation was avoided during the procedure to keep the cells in the dark-adapted state. Irradiation of all the aliquots with white LED light at an intensity of 200±10 µmol $m^{-2}s^{-1}$ or 30±2 µmol $m^{-2}s^{-1}$ was initiated, followed by sampling of the cells at the indicated time points by adding into 750 µL PCI supplemented with ^{13}C-IS dissolved in 20 µL water (for absolute concentration analysis) or with 5 µL of 0.5 M CAPS (pH 10.6) (for ^{13}C incorporation analysis). The cell suspension before illumination was extracted as the nominal 0-s sample. To precisely determine the amount of extracted cells, the OD_{730} of the final cell suspension was measured. After the extraction mixtures were centrifuged at 4 ºC at 12,000×*g* for 2 min, harvested aliquots of the water layer were lyophilized.

The lyophilized samples were dissolved in 20 µL of 0.4 mM piperazine-1,4-bis(2-ethanesulfonic acid) (PIPES) and analyzed by CE-MS as described above. Absolute concentrations of each metabolite (*C'*) were derived as follows:

$$C' = \frac{S'_0}{WS'_n} C_n V \tag{4}$$

where, S'_0 and S'_n are the peak areas of unlabeled and uniformly ^{13}C-labeled IS signals, respectively, *W* represents DCW, and *V* is the sample volume for CE-MS analysis. ^{13}C fractions were calculated as described previously (34).

Short-term dynamic metabolic flux analysis (STD-MFA)

To estimate the temporal changes of 18 fluxes in the metabolic map shown in *SI Appendix*, Fig. S8, 18 metabolite accumulation rates r_i(t) in equation (1) were derived from the slope taken between two consecutive concentration data points shown in Fig. 2. Accumulation rates of metabolites under the detection limit (E4P, R5P, GAP <0.001 nmol/mg DCW) and peak-unidentified metabolites (BPG and SBP) were set to zero. In addition, the CO_2 fixation rate derived from the slope taken between two consecutive data points shown in *SI Appendix*, Fig. S3*C* and *D* was regarded as the metabolic flux of Rubisco (i.e., the conversion of RuBP to 3PG). The set of 19 equations, including the 18 unknown fluxes in the network, was represented in matrix notation as follows:

$$\mathbf{A}\mathbf{x}(\mathrm{t}) = \mathbf{r}(t) \tag{5}$$

where, A is the 19 × 18 matrix of stoichiometric coefficients, **x**(t) is the 18-dimensional flux vector, and r(t) is the 19-dimensional metabolite accumulation rate vector. The specific form of equation (4) is shown in *SI Appendix*, Fig. S8*B*. The weighted least squares solution to equation (5) is as follows:

$$\hat{\mathbf{x}}(\mathrm{t}) = (\mathbf{A}^T\mathbf{W}\mathbf{A})^{-1}\mathbf{A}^T\mathbf{W}\bar{\mathbf{r}}(t) \tag{6}$$

where, the superscripts ˆ and ¯ denote estimated and measured quantities (respectively), and **W** is a 19-dimensional weighting diagonal matrix, whose diagonal elements are the reciprocal of the variance of the measured metabolic accumulation rate values. Variance values for the accumulation rate of E4P, R5P, GAP, BPG and SBP, and for the CO_2 fixation rate, were set to 10^{-15} (i.e., a value that was effectively zero). To evaluate the reliability of the estimated fluxes, the metabolite accumulation rates were calculated as follows:

$$\mathbf{A}\hat{\mathbf{x}}(t) = \hat{\mathbf{r}}(t) \quad (7)$$

The estimated and measured metabolite accumulation rate values are compared in *SI Appendix*, Fig. S9.

Oxygen evolution measurement

Synechocystis wild-type cells were collected and re-suspended in the same way as the preparation process in the metabolite sampling experiment described above. Whole-cell oxygen evolution was measured with light illumination at intensities of 200 µmol $m^{-2}s^{-1}$ or 30 µmol $m^{-2}s^{-1}$ in a Clark-type oxygen electrode (Hansatech Instruments) containing 750 µL of the cell suspension.

Acknowledgments

This work was supported by the Mirai Program [grant number JPMJMI19E4] from the Japan Science and Technology Agency (JST) of the Ministry of Education, Culture, Sports, Science, and Technology (MEXT), Japan, and the Japan Society for the Promotion of Science (JSPS) Kakenhi (Grants-in-Aid for Scientific Research) Grant Number 21J00113.

References

1. D. A. Walker, Photosynthetic induction phenomena and the light activation of ribulose diphosphate carboxylase. *New Phytol.* 72, 209–235 (1973).
2. W. J. Osterhout, A. R. Haas, Dynamical Aspects of Photosynthesis. *Proc. Natl. Acad. Sci. USA.* 4, 85–91 (1918).
3. B. B. Buchanan, Role of light in the regulation of chloroplast enzymes. *Ann. Rev. Plant Physiol.* 31, 341–374 (1980).
4. G. H. Lorimer, M. R. Badger, T. J. Andrews, The Activation of Ribulose-1,5,-bisphosphate carboxylase by carbon dioxide and magnesium ions. Equilibria, kinetics, a suggested mechanisms, and physiological implications. *Biochem*. 15, 529–536 (1976).
5. A. R. Portis, Jr., The regulation of Rubisco by Rubisco activase. *J. Exp. Bot.* 46, 1285–1291 (1995).
6. L. Michelet, et al. Redox regulation of the Calvin-Benson cycle: something old, something new. *Front Plant Sci* 4, 470 (2013).
7. R. W. Pearcy, J. P. Krall, G. F. Sassenrath-Cole, Photosynthesis in Fluctuating Light Environments. In: Baker NR, ed. *Photosynthesis and the Environment.* Dordrecht: Kluwer, 321–346 (1996).
8. A. Matuszyńska, N. P. Saadat, O. Ebenhöh, Balancing energy supply during photosynthesis - a theoretical perspective. *Physiol. Plant* 166, 392–402 (2019).
9. G. Shimakawa, et al. Respiration accumulates Calvin cycle intermediates for the rapid start of photosynthesis in *Synechocystis* sp. PCC 6803. *Biosci. Biotechnol. Biochem.* 78, 1997–2007 (2014).
10. S. Shinde, et al. Glycogen Metabolism Supports Photosynthesis Start through the Oxidative Pentose Phosphate Pathway in Cyanobacteria. *Plant Physiol.* 182, 507–517 (2020).
11. J. A. Bassham, K. Shibata, K. Steenberg, J. Bourdon, M. Calvin, The photosynthetic cycle and respiration: Light-dark transients. *J. Am. Chem. Soc.* 78, 4120–4124 (1956).
12. M. Stitt, W. Wirtz, H. W. Heldt, Metabolite levels during induction in the chloroplast and extrachloroplast compartments of spinach protoplasts. *Biochim. Biophys. Acta.* 593, 85–102 (1980).
13. R. C. Leegood, R. T. Furbank, Carbon metabolism and gas exchange in leaves of Zea mays L.: Changes in CO_2 fixation, chlorophyll a fluorescence and metabolite levels during photosynthetic induction. *Planta.* 162, 450–456 (1984).
14. H. Usuda, Changes in Levels of Intermediates of the C(4) Cycle and Reductive Pentose Phosphate Pathway during Induction of Photosynthesis in Maize Leaves. *Plant Physiol.* 78,

859–864 (1985).
15. J. Kobza, G. E. Edwards, The photosynthetic induction response in wheat leaves: net CO_2 uptake, enzyme activation, and leaf metabolites. *Planta* 171, 549–559 (1987).
16. M. Janasch, J. Asplund-Samuelsson, R. Steuer, E. P. Hudson, Kinetic modeling of the Calvin cycle identifies flux control and stable metabolomes in *Synechocystis* carbon fixation. *J. Exp. Bot.* 70, 973–983 (2019).
17. R. I. Ponce-Toledo, et al. An Early-Branching Freshwater Cyanobacterium at the Origin of Plastids. *Curr. Biol.* 27, 386–391 (2017).
18. H. Shimizu, Y. Toya, Recent advances in metabolic engineering-integration of in silico design and experimental analysis of metabolic pathways. *J. Biosci. Bioeng.* 132, 429–436 (2021).
19. U. Sauer, Metabolic networks in motion: ^{13}C-based flux analysis. *Mol. Syst. Biol.* 2, 62 (2006).
20. R. W. Leighty, M. R. Antoniewicz, Dynamic metabolic flux analysis (DMFA): a framework for determining fluxes at metabolic non-steady state. *Metab. Eng.* 13, 745–755 (2011).
21. J. Niklas, E. Schräder, V. Sandig, T. Noll, E. Heinzle, Quantitative characterization of metabolism and metabolic shifts during growth of the new human cell line AGE1.HN using time resolved metabolic flux analysis. *Bioprocess Biosyst. Eng.* 34, 533–545 (2011).
22. J. J. Vallino, G. Stephanopoulos, Metabolic flux distributions in *Corynebacterium glutamicum* during growth and lysine overproduction. *Biotechnol. Bioeng.* 41, 633–646 (1993).
23. F. R. Pinu, S. G. Villas-Boas, R. Aggio, Analysis of Intracellular Metabolites from Microorganisms: Quenching and Extraction Protocols. *Metabolites.* 7, E53 (2017).
24. J. D. Rabinowitz, E. Kimball, Acidic acetonitrile for cellular metabolome extraction from Escherichia coli. *Anal. Chem.* 79, 6167–6173 (2007).
25. T. M. Annesley, Ion suppression in mass spectrometry. *Clin. Chem.* 49, 1041-1044 (2003).
26. K. Tanaka, et al. Quantification of NAD(P)H in cyanobacterial cells by a phenol extraction method. *Photosynth. Res.* 148, 57–66 (2021).
27. G. Shimakawa, et al. FLAVODIIRON2 and FLAVODIIRON4 proteins mediate an oxygen-dependent alternative electron flow in *Synechocystis* sp. PCC 6803 under CO_2-limited conditions. *Plant. Physiol.* 167, 472–480 (2015).
28. L. Wu, et al. Quantitative analysis of the microbial metabolome by isotope dilution mass spectrometry using uniformly ^{13}C-labeled cell extracts as internal standards. *Anal. Biochem.* 336, 164–171 (2005).
29. B. D. Bennett, et al. Absolute metabolite concentrations and implied enzyme active site occupancy in *Escherichia coli*. *Nat. Chem. Biol.* 5, 593–599 (2009).
30. Y. Dempo, E. Ohta, Y. Nakayama, T. Bamba, E. Fukusaki, Molar-based targeted metabolic profiling of cyanobacterial strains with potential for biological production. *Metabolites.* 4, 499–516 (2014).
31. S. Nishino, N. Okahashi, F. Matsuda, H. Shimizu, Absolute quantitation of glycolytic intermediates reveals thermodynamic shifts in *Saccharomyces cerevisiae* strains lacking *PFK1* or *ZWF1* genes. *J. Biosci. Bioeng.* 120, 280–286 (2015).
32. J. Kauny, P. Sétif, NADPH fluorescence in the cyanobacterium *Synechocystis* sp. PCC 6803: a versatile probe for in vivo measurements of rates, yields and pools. *Biochim. Biophys. Acta.* 1837, 792–801 (2014).
33. S. H. Yoo, B. H. Lee, Y. Moon, M. H. Spalding, J. L. Jane, Glycogen synthase isoforms in *Synechocystis* sp. PCC6803: identification of different roles to produce glycogen by targeted mutagenesis. *PLoS One.* 9, e91524 (2014).
34. T. Hasunuma, M. Matsuda, Y. Kato, C. J. Vavricka, A. Kondo, Temperature enhanced succinate production concurrent with increased central metabolism turnover in the cyanobacterium *Synechocystis* sp. PCC 6803. *Metab. Eng.* 48, 109–120 (2018).
35. M. Tamoi, T. Takeda, S. Shigeoka, Functional analysis of Fructose-1,6-bisphosphatase isozymes (*fbp-I* and *fbp-II* gene products) in cyanobacteria. *Plant Cell Physiol.* 40, 257–261 (1999).

36. A. G. Miller, D. T. Canvin, Glycolaldehyde Inhibits CO_2 Fixation in the Cyanobacterium *Synechococcus* UTEX 625 without Inhibiting the Accumulation of Inorganic Carbon or the Associated Quenching of Chlorophyll *a* Fluorescence. *Plant. Physiol.* 91, 1044–1049 (1989).
37. Y. Tsukamoto, Y. Fukushima, S. Hara, T. Hisabori, Redox control of the activity of phosphoglycerate kinase in *Synechocystis* sp. PCC6803. *Plant Cell. Physiol.* 54, 484–491 (2013).
38. C. R. McFarlane, et al. Structural basis of light-induced redox regulation in the Calvin-Benson cycle in cyanobacteria. *Proc. Natl. Acad. Sci. USA.* 116, 20984-20990 (2019).
39. L. Feng, et al. Structural and biochemical characterization of fructose-1,6/sedoheptulose-1,7-bisphosphatase from the cyanobacterium *Synechocystis* strain 6803. *FEBS J.* 281, 916–926 (2014).
40. M. J. Mallén-Ponce, M. J. Huertas, A. M. Sánchez-Riego, F. J. Florencio, Depletion of m-type thioredoxin impairs photosynthesis, carbon fixation, and oxidative stress in cyanobacteria. *Plant Physiol.* 187, 1325–1340 (2021).
41. F. Liang, P. Lindblad, Effects of overexpressing photosynthetic carbon flux control enzymes in the cyanobacterium *Synechocystis* PCC 6803. *Metab. Eng.* 38, 56–64 (2016).
42. Y. Marcus, M. Gurevitz, Activation of cyanobacterial RuBP-carboxylase/oxygenase is facilitated by inorganic phosphate via two independent mechanisms. *Eur. J. Biochem.* 267, 5995–6003 (2000).
43. J. T. Perchorowicz, D. A. Raynes, R. G. Jensen, Light limitation of photosynthesis and activation of ribulose bisphosphate carboxylase in wheat seedlings. *Proc. Natl. Acad. Sci. USA.* 78, 2985–2989 (1981).
44. J. R. Seemann, M. U. Kirschbaum, T. D. Sharkey, R. W. Pearcy, Regulation of Ribulose-1,5-Bisphosphate Carboxylase Activity in *Alocasia macrorrhiza* in Response to Step Changes in Irradiance. *Plant Physiol.* 88, 148–152 (1988).
45. S. Ito, T. Osanai, Unconventional biochemical regulation of the oxidative pentose phosphate pathway in the model cyanobacterium *Synechocystis* sp. PCC 6803. *Biochem. J.* 477, 1309–1321 (2020).
46. D. Christodoulou, et al. Reserve Flux Capacity in the Pentose Phosphate Pathway Enables *Escherichia coli*'s Rapid Response to Oxidative Stress. *Cell Syst.* 6, 569–578.e7 (2018).
47. M. Maruyama, et al. Time-resolved analysis of short term metabolic adaptation at dark transition in *Synechocystis* sp. PCC 6803. *J. Biosci. Bioeng.* 128, 424–428 (2019).
48. S. Gleizer, et al. Conversion of Escherichia coli to Generate All Biomass Carbon from CO_2. *Cell.* 179, 1255–1263.e12 (2019).
49. T. Gassler, et al. The industrial yeast Pichia pastoris is converted from a heterotroph into an autotroph capable of growth on CO_2. *Nat. Biotechnol.* 38, 210–216 (2020).
50. J. G. K. Williams, Construction of specific mutations in photosystem II photosynthetic reaction center by genetic engineering methods in *Synechocystis* 6803. *Methods Enzymol.* 167, 766–778 (1988).
51. T. Hasunuma, et al. Dynamic metabolic profiling of cyanobacterial glycogen biosynthesis under conditions of nitrate depletion. *J. Exp. Bot.* 64, 2943–2954 (2013).

Figures and Tables

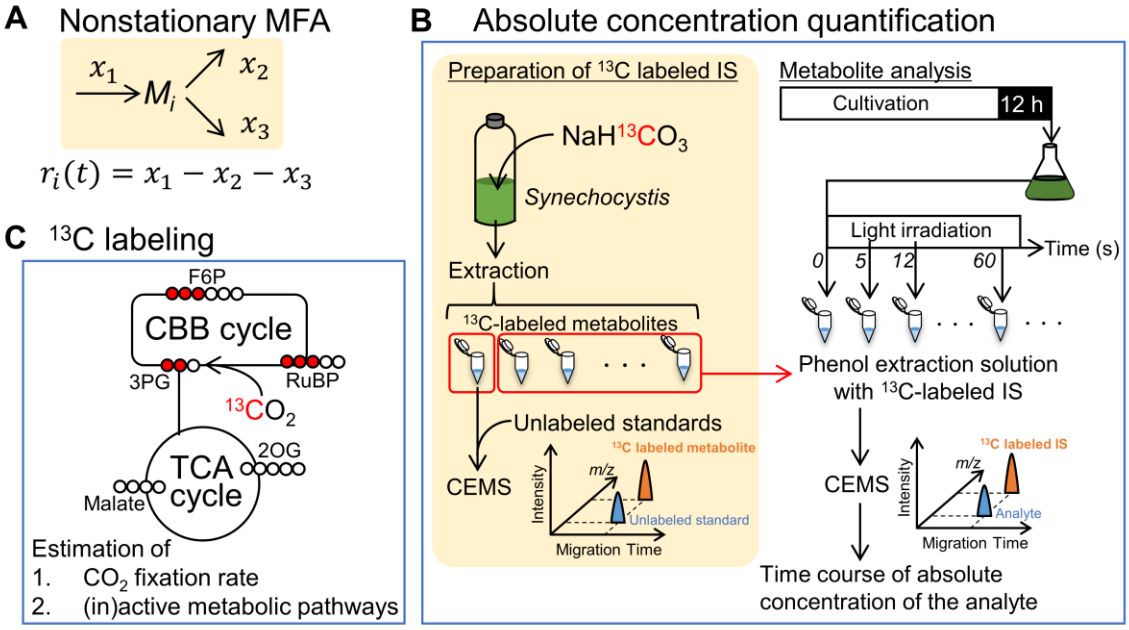

Figure 1. Process for estimating temporal changes in metabolic flux. (*A*) Relationship between concentration change and metabolic flux. r_i(t) is the accumulation rate of metabolite M_i. x_n represents the metabolic flux of the *n*th reaction. (*B*) Experimental procedure for quantifying absolute metabolite concentration. (*C*) Schematic example of isotope-labeled state during $^{13}CO_2$ incorporation. Empty and red-filled circles represent unlabeled and labeled carbon atoms, respectively. Abbreviations: CBB, Calvin-Benson-Bassham; CEMS, capillary electrophoresis-mass spectrometry; F6P, fructose 6-phosphate; IS, internal standard; RuBP, ribulose 1,5-bisphosphate; TCA, tricarboxylic acid; 2OG, 2-oxoglutarate; 3PG, 3-phosphoglycerate.

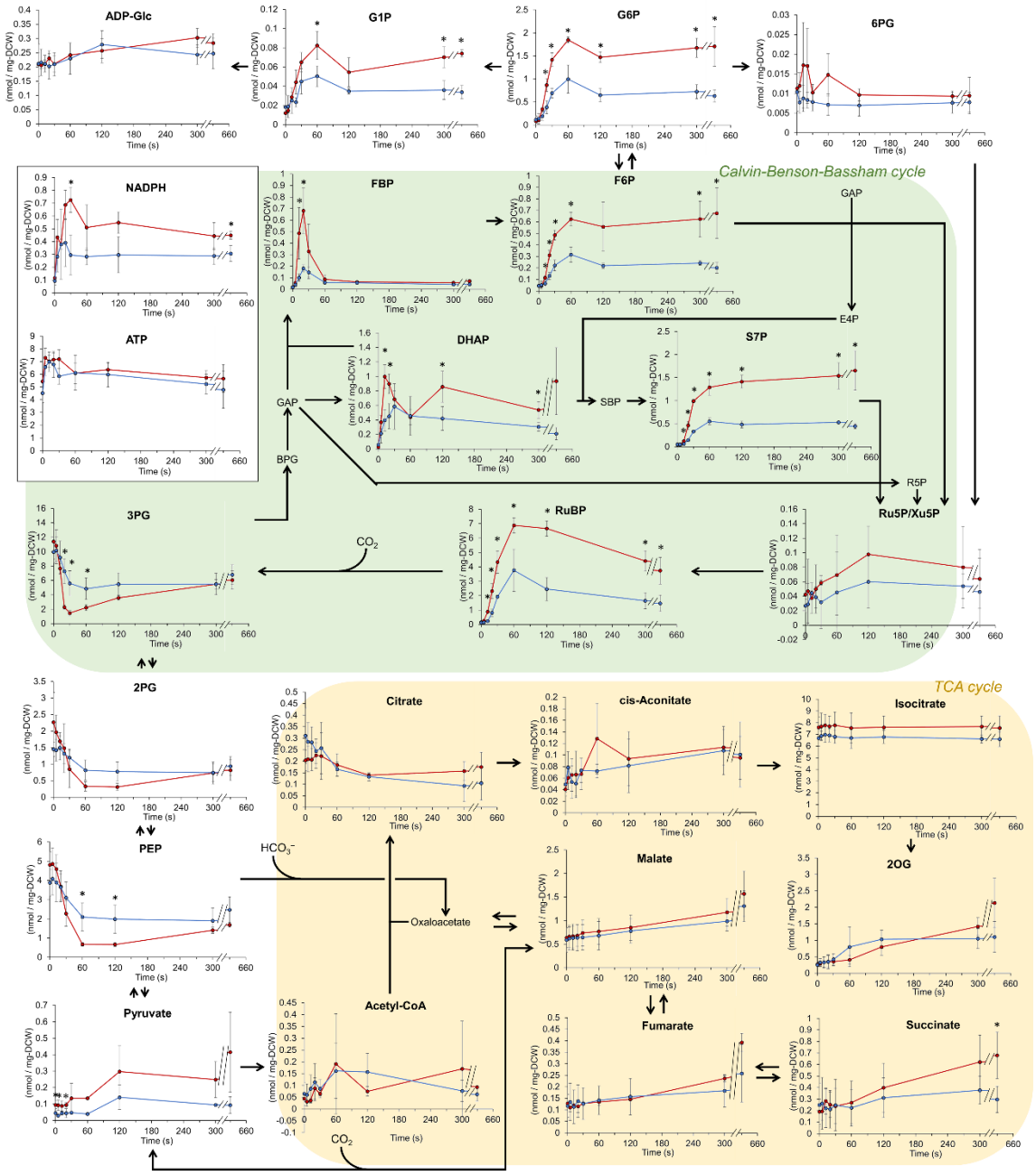

Figure 2. Rapid temporal changes in absolute metabolite concentration during the start of photosynthesis. Intracellular metabolites were extracted at the indicated times after transition from darkness to light-irradiated condition at light intensities of 200 μmol m^{-2} s^{-1} (red line) or 30 μmol m^{-2} s^{-1} (blue line). Levels of glyceraldehyde 3-phosphate (GAP), erythrose 4-phosphate (E4P), and ribose 5-phosphate (R5P) were below the detection limit (0.001 nmol/mg DCW). 1,3-Bisphosphoglycerate (BPG) and sedoheptulose 1,7-bisphosphate (SBP) were not identified due to lack of commercial reagent for use as a standard. Black arrows indicate metabolic pathways. Abbreviations: DCW, dry cell weight; DHAP, dihydroxyacetone phosphate; FBP, fructose 1,6-bisphosphate; F6P, fructose 6-phosphate; G1P, glucose 1-phosphate; G6P, glucose 6-phosphate; 2OG, 2-oxoglutarate; PEP, phosphoenolpyruvate; 6PG, 6-phosphogluconate; 2PG, 2-phosphoglycerate; 3PG, 3-phosphoglycerate; RuBP, ribulose 1,5-bisphosphate; Ru5P, ribulose

5-phosphate; S7P, sedoheptulose 7-phosphate; Xu5P, Xylulose 5-phosphate. Values are the mean ± SD (bars) of three independent experiments. Significant differences between the two light intensities were evaluated by a two-tailed non-paired Student's t test (* $p < 0.05$).

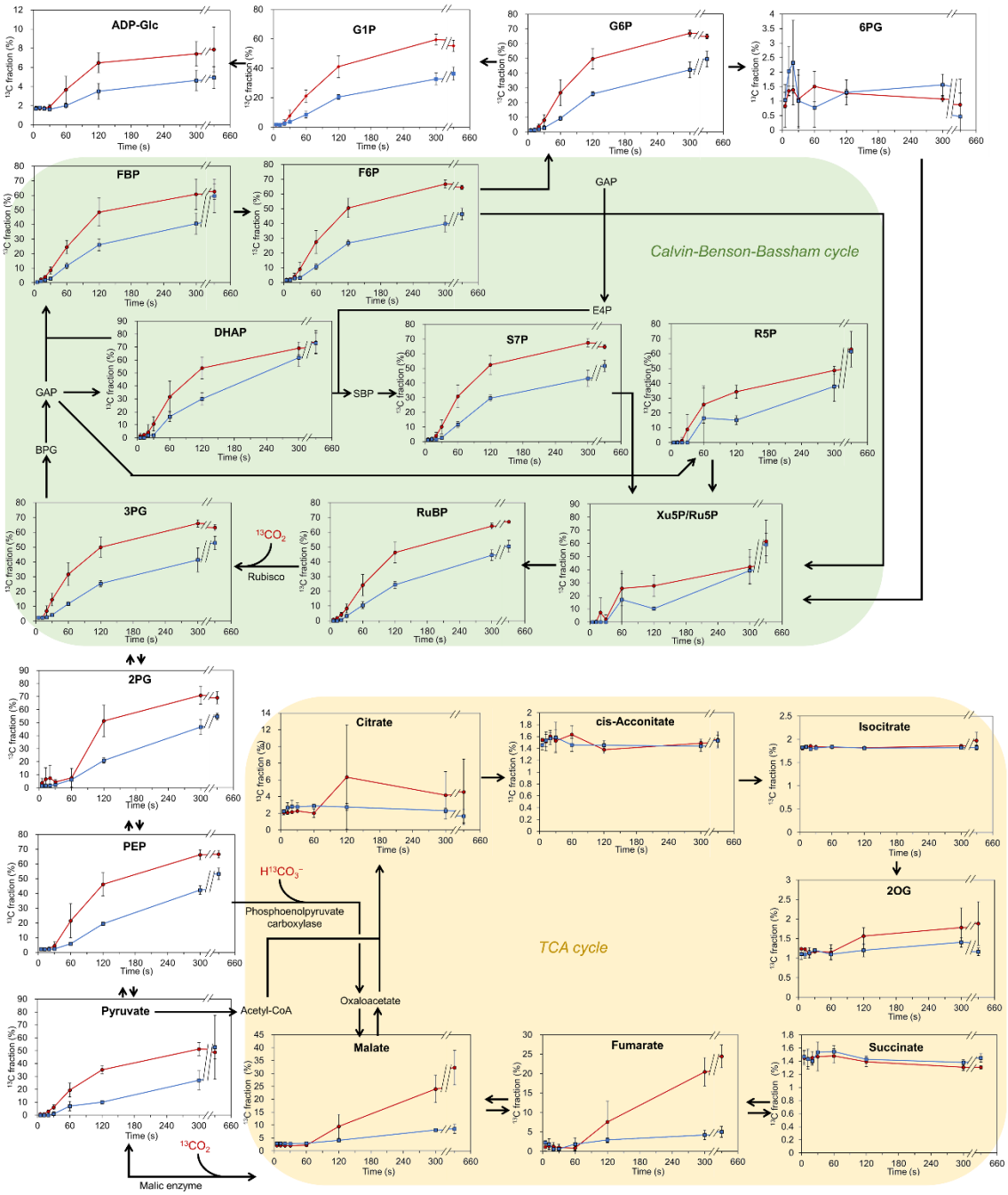

Figure 3. Time course of ^{13}C fraction of metabolites following light irradiation at 200 μmol m^{-2} s^{-1} (red line) or 30 μmol m^{-2} s^{-1} (blue line). Values are the mean ± SD (bars) of three biological replicates. Black arrows indicate metabolic pathways. Abbreviations are the same as in the Figure 2 legend.

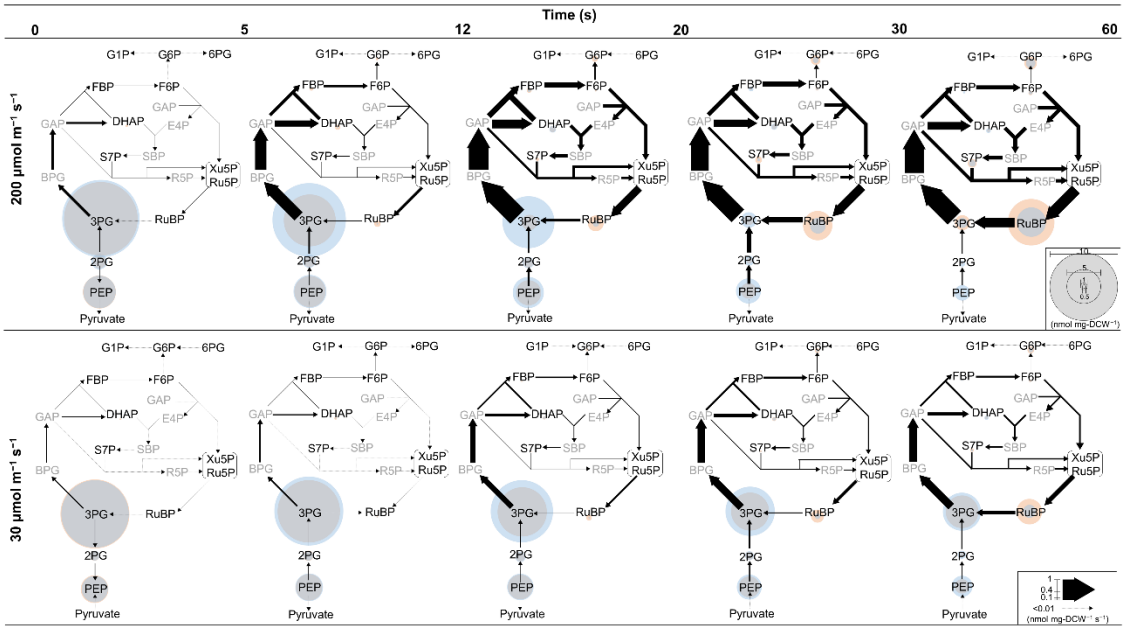

Figure 4. Estimated change in metabolic flux after initiating light irradiation at 200 µmol m^{-2} s^{-1} (upper row) and 30 µmol m^{-2} s^{-1} (lower row). Metabolic fluxes are indicated by the thickness of arrows with values indicated by the scale bar in the lower right corner. Metabolite concentrations at the beginning and end of each time interval are indicated by the diameters of blue and orange circles, respectively. Overlap between orange and blue circles (namely invariant concentration during a time interval) is shown in gray. Abbreviations are the same as in the Figure 2 legend.

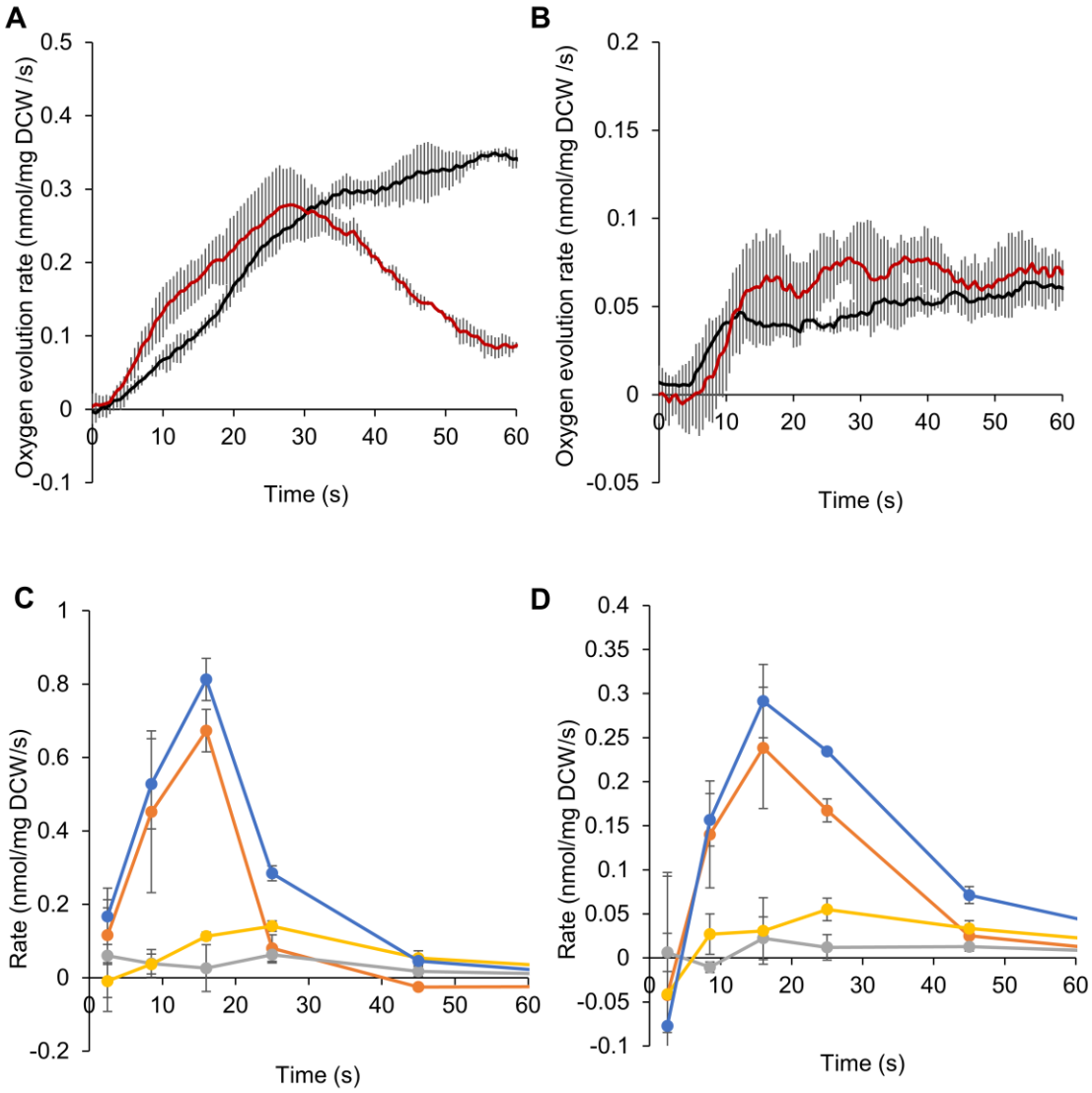

Figure 5. Oxygen evolution rate in the presence of glycolaldehyde (GA) and comparison with metabolite variation rate. (*A, B*) Oxygen evolution rate in the absence (black line) and presence (red line) of GA after light irradiation at intensities of 200 μmol m^{-2} s^{-1} (*A*) or 30 μmol m^{-2} s^{-1} (*B*). GA (10 mM) was added before the initiation of light irradiation. (*C, D*) Decreasing rate of 3PG (orange line), PEP (yellow line), and 2PG (gray line), and the sum of these three metabolites (blue line) after initiation of light irradiation at the intensity of 200 μmol m^{-2} s^{-1} (*C*) or 30 μmol m^{-2} s^{-1} (*D*). Since the decreasing rates were derived from two consecutive concentration data points, values are plotted at a time point representing the average (mean) of the two time points. For all panels, values are plotted as the mean ± SD (bars) of three biological replicates. Abbreviations are the same as in the Figure 2 legend.